PHYSICAL REVIEW D **96,** 094508 (2017)

Nucleon transverse momentum-dependent parton distributions in lattice QCD: Renormalization patterns and discretization effects

Boram Yoon,[1] Michael Engelhardt,[2] Rajan Gupta,[1] Tanmoy Bhattacharya,[1] Jeremy R. Green,[3] Bernhard U. Musch,[4] John W. Negele,[5] Andrew V. Pochinsky,[5] Andreas Schäfer,[4] and Sergey N. Syritsyn[6,7]

[1]*Los Alamos National Laboratory, Theoretical Division T-2, Los Alamos, New Mexico 87545, USA*
[2]*Department of Physics, New Mexico State University, Las Cruces, New Mexico 88003-8001, USA*
[3]*NIC, Deutsches Elektronen-Synchrotron, 15738 Zeuthen, Germany*
[4]*Institut für Theoretische Physik, Universität Regensburg, 93040 Regensburg, Germany*
[5]*Center for Theoretical Physics, Massachusetts Institute of Technology, Cambridge, Massachusetts 02139, USA*
[6]*Department of Physics and Astronomy, Stony Brook University, Stony Brook, New York 11794, USA*
[7]*RIKEN/BNL Research Center, Brookhaven National Laboratory, Upton, New York 11973, USA*

(Received 15 June 2017; published 21 November 2017)

Lattice QCD calculations of transverse momentum-dependent parton distribution functions (TMDs) in nucleons are presented, based on the evaluation of nucleon matrix elements of quark bilocal operators with a staple-shaped gauge connection. Both time-reversal odd effects, namely, the generalized Sivers and Boer-Mulders transverse momentum shifts, as well as time-reversal even effects, namely, the generalized transversity and one of the generalized worm-gear shifts, are studied. Results are obtained on two different $n_f = 2 + 1$ flavor ensembles with approximately matching pion masses but very different discretization schemes: domain-wall fermions (DWF) with lattice spacing $a = 0.084$ fm and pion mass 297 MeV, and Wilson-clover fermions with $a = 0.114$ fm and pion mass 317 MeV. Comparison of the results on the two ensembles yields insight into the length scales at which lattice discretization errors are small, and into the extent to which the renormalization pattern obeyed by the continuum QCD TMD operator continues to apply in the lattice formulation. For the studied TMD observables, the results are found to be consistent between the two ensembles at sufficiently large separation of the quark fields within the operator, whereas deviations are observed in the local limit and in the case of a straight link gauge connection, which is relevant to the studies of parton distribution functions. Furthermore, the lattice estimates of the generalized Sivers shift obtained here are confronted with, and are seen to tend towards, a phenomenological estimate extracted from experimental data.

DOI: 10.1103/PhysRevD.96.094508

I. INTRODUCTION

An important aspect of nucleon internal dynamics is the three-dimensional momentum carried by quarks, comprising not only the longitudinal momentum fraction x encoded in standard parton distribution functions, but also momentum in the transverse plane. It is characterized by transverse momentum-dependent parton distribution functions (TMDs). TMDs enter in, for example, angular asymmetries measured in semi-inclusive deep inelastic scattering (SIDIS) processes of electrons off nucleons. Depending on the polarizations of the nucleon and the struck quark, a number of correlations can be studied, including the time-reversal odd (T-odd) effects encoded in the Sivers [1] and Boer-Mulders [2] TMDs. These are a consequence of final state interactions in the SIDIS process, and analogously manifest themselves via initial state interactions in the Drell-Yan (DY) process. TMDs are a focus of experiments at the JLab 12 GeV facility [3,4] and at RHIC [5], and constitute an important component of the motivation for the proposed electron-ion collider (EIC) [6].

To obtain first-principles, nonperturbative input for the theoretical study of TMDs, a method to evaluate TMD observables in lattice QCD has been developed and explored in [7–9]. In the present work, we report results obtained on two gauge ensembles at approximately matching pion masses, but with substantially differing fermion discretization schemes: one is a $2 + 1$-flavor RBC/UKQCD domain-wall fermion ensemble with lattice spacing $a = 0.084$ fm and pion mass 297 MeV [10]; the other is a $2 + 1$-flavor isotropic clover fermion ensemble generated by R. Edwards, B. Joó and K. Orginos [11] with lattice spacing $a = 0.114$ fm and pion mass 317 MeV. Aside from being located closer to the physical pion mass than the aforementioned previous investigations, the availability of data on these two separate ensembles allows us to investigate two specific facets of the lattice TMD calculational scheme pursued here; namely, discretization effects and the renormalization of the quark bilocal operators used in the definition and evaluation of TMDs, laid out in detail in Sec. II.

The composite operator used to extract TMDs consists of a quark and an antiquark field connected by an intrinsically

nonlocal gauge connection—a path ordered product of gauge links. The divergences associated with the quantum fluctuations of the latter are absorbed into a multiplicative "soft factor" in the continuum QCD scheme developed in Refs. [12,13].[1] In addition, renormalization factors are attached to the quark fields. This multiplicative nature of renormalization in continuum QCD is central to the construction of the TMD observables considered here, in which the renormalization factors are canceled by forming suitable ratios. Whether this multiplicative nature of renormalization carries over into the lattice framework is, however, a point which demands further investigation. One possible manifestation of the violation of multiplicativity would be if results for the aforementioned TMD ratios vary with the lattice discretization scheme, and the difference persists as the lattice spacing is taken to zero.

The availability of lattice TMD data on two ensembles with approximately matching pion masses, but differing discretizations provides an opportunity for an empirical test of the universality of TMD ratios. This is a primary focus of the present work. One would expect that the lattice operators approximate the continuum operators well at finite physical extent, and that results obtained on the two ensembles therefore match. On the other hand, the local limit may exhibit additional ultraviolet divergences, as well as signatures of operator mixing attributable to the breaking of continuum symmetries, such as rotational symmetry and, in the case of clover fermions, chiral symmetry. It is well known that in the local limit, renormalization constants of composite operators become dependent on the Dirac structure, whereas the soft factors and quark wave function renormalizations used to renormalize the nonlocal TMD operators do not depend on the Dirac structure. The working assumption underlying the construction of the TMD observables considered in this work is that, at large enough separation, the renormalization factors become independent of the Dirac structure and cancel in ratios. Comparing the results obtained on the two ensembles is expected to uncover whether, at what length scales, and under what conditions this assumption holds, and whether any signatures of deviations from this simple renormalization pattern can be detected.

This paper is organized as follows. Section II lays out the definition of TMDs and the construction of TMD ratio observables in which multiplicative soft factors and renormalization constants cancel. Particulars of the lattice QCD evaluation of these quantities are given in Sec. III. Results for the Sivers shift, Boer-Mulders shift, transversity h_1 and the g_{1T} worm-gear shift are given in Sec. IV. Some results pertinent to the calculation of parton distribution functions (PDFs) are given in Sec. IV E. A comparison of our estimate of the generalized Sivers shift with that extracted from SIDIS experiments is presented in Sec. V. Conclusions are given in Sec. VI.

[1]Throughout this paper, the label "soft factor" denotes both soft and collinear divergences.

II. CONSTRUCTION OF TMD OBSERVABLES

The calculational scheme employed to arrive at lattice TMD observables has been laid out in detail in [9]; cf. also [7,8]. The following synopsis emphasizes, in particular, how multiplicative soft factors enter the scheme, and the consequent construction of TMD ratios in which these factors cancel. TMDs are derived from the fundamental correlator

$$\tilde{\Phi}^{[\Gamma]}_{\text{unsubtr}}(b,P,S,\ldots) \equiv \frac{1}{2}\langle P,S|\bar{q}(0)\Gamma\mathcal{U}[0,\eta v,\eta v+b,b]q(b)|P,S\rangle \quad (1)$$

where the subscript "unsubtr." indicates that no provision has been made yet to absorb ultraviolet and soft divergences into appropriate renormalization factors. The nucleon states are characterized by the longitudinal momentum P and the spin S. We will consistently use the tilde, as in $\tilde{\Phi}$, to denote position space correlation functions and the same symbols without the tilde for their Fourier transforms. The quark fields, separated by a displacement b, are connected by the gauge connection $\mathcal{U}[0,\eta v,\eta v+b,b]$, the arguments of which denote space-time positions connected by path-ordered products of gauge links approximating straight Wilson lines. The full gauge connection thus has the shape of a staple, with the direction of the staple encoded in the vector v, and its length in the scalar η as shown in Fig. 1. We are specifically interested in the limit $|\eta| \to \infty$, in which this gauge connection represents gluon exchange in semi-inclusive deep inelastic scattering (SIDIS) and Drell-Yan (DY) processes. The directions of the staples in the two cases are opposite to one another; in the SIDIS case, the staple-shaped gauge connection incorporates final state

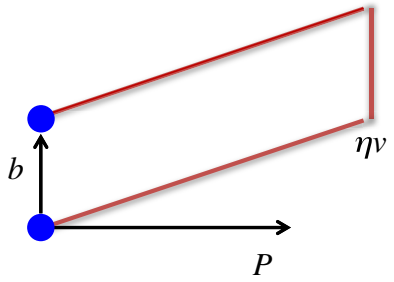

FIG. 1. Illustration of the TMD operator with staple-shaped gauge connection. The four-vectors v and P give the direction of the staple and the momentum, while b defines the separation between the quark operators. The values of these variables used in the lattice calculation are given in Table II. In the present calculation, $b \cdot P = b \cdot v = 0$ is chosen, corresponding to evaluating the first moment of the TMDs with respect to the quark momentum fraction x.

interactions of the struck quark, whereas in the DY case, it incorporates initial state interactions.

An additional important specification regarding the concrete choice of the staple direction v is needed. In the definition of TMDs, v is taken to have no transverse component, $\boldsymbol{v}_{\mathrm{T}} = 0$. Furthermore, in a hard scattering process, the rapidity difference between the incoming hadron and the struck quark is very large, and a natural choice for v would therefore be a light-cone vector. However, such a choice leads to severe rapidity divergences beyond tree level [14], which are regulated by taking v off the light cone into the spacelike region. Consequently, TMDs depend on an additional Collins-Soper type parameter $\hat{\zeta}$ characterizing how close v is to the light cone,

$$\hat{\zeta} = \frac{v \cdot P}{\sqrt{|v^2|}\sqrt{P^2}}. \tag{2}$$

The light-cone limit corresponds to $\hat{\zeta} \to \infty$. Note that this limit can be approached even with a purely spatial choice of v, as used in lattice calculations, by making the spatial momentum $\boldsymbol{P}$ large. For a given $|\boldsymbol{P}|$, the maximum of $v \cdot P$ is obtained by choosing $\boldsymbol{P}$ to be aligned with the staple direction $\boldsymbol{v}$. In that case $\hat{\zeta} = |\boldsymbol{P}|/m_N$. In practice, lattice QCD calculations only access a fairly limited range of $\hat{\zeta}$ because of limitations in performing simulations at large $\boldsymbol{P}$; ultimately, one aims to connect to the region of sufficiently large values in which perturbative evolution equations become applicable [12,15]. At this time, perturbative evolution formulas for the specific quantities we study are not available; having them would be useful to constrain the form of the high $\hat{\zeta}$ behavior. A dedicated lattice study of the $\hat{\zeta}$-scaling of a TMD observable was performed in [16]. A perspective for extending lattice TMD calculations to higher nucleon momenta, and therefore higher $\hat{\zeta}$, is given by the recently developed momentum smearing method described in [17].

To regulate the TMD correlator defined in Eq. (1), one considers subtracted correlation functions [12,13]

$$\tilde{\Phi}^{[\Gamma]}_{\mathrm{subtr}}(b, P, S, \ldots) = \tilde{\Phi}^{[\Gamma]}_{\mathrm{unsubtr}}(b, P, S, \ldots) \cdot \mathcal{S} \cdot Z_{\mathrm{TMD}} \cdot Z_2, \tag{3}$$

in which divergences have been absorbed into three separate factors: $\mathcal{S}$ regulates the soft and collinear divergences associated with the gauge connection, Z_2 is the quark field renormalization factor, and the rest, Z_{TMD}, contains the dependence on the specific tensor structure of the TMD operator under consideration. As discussed in Refs. [12,13], the factor $\mathcal{S}$ is defined only in terms of Wilson lines, and Z_2 is also independent of the particular choice of the TMD operator. In Eqs. (21), (22), (23), and (24), we define the four observables we calculate as ratios, in which the unpolarized TMD moment $\tilde{f}_1^{[1](0)}$ [cf. Eqs. (5) and (19)] is used to define the denominator. The reason for studying ratios rests on the assumption that the full renormalization $\mathcal{Z}$ continues to factor in the lattice formulation; i.e., the renormalization pattern given in Eq. (3) with $\mathcal{Z} = \mathcal{S} \cdot Z_{\mathrm{TMD}} \cdot Z_2$ also holds on the lattice. In that case, the two factors $\mathcal{S} \cdot Z_2$ would cancel in the ratios. The additional assumption is that for finite physical separation, b, the factor Z_{TMD} becomes independent of the spin (γ-matrix) structure of the TMD operator, and therefore it also cancels in the ratio. Note that, at finite lattice cutoff, there is no hard separation between the local limit and finite physical distances, and a smooth transition in behavior occurs over several lattice spacings. A similar multiplicative renormalization is used to regulate the operator used in studies of PDFs [18–21].

The analysis of TMDs in the continuum is in terms of the subtracted correlation function $\tilde{\Phi}^{[\Gamma]}_{\mathrm{subtr}}$, which upon Fourier transformation yields the momentum space correlator

$$\Phi^{[\Gamma]}(x, \boldsymbol{k}_T, P, S, \ldots) = \int \frac{d^2\boldsymbol{b}_{\mathrm{T}}}{(2\pi)^2} \int \frac{d(b \cdot P)}{2\pi P^+} e^{ix(b\cdot P) - i\boldsymbol{b}_{\mathrm{T}}\cdot\boldsymbol{k}_{\mathrm{T}}} \tilde{\Phi}^{[\Gamma]}_{\mathrm{subtr}}|_{b^+=0}, \tag{4}$$

in which the suppressed momentum component k^- is integrated over, leading to the specification $b^+ = 0$. The transverse components $\boldsymbol{b}_{\mathrm{T}}$ of the quark separation b are Fourier conjugate to the quark transverse momentum $\boldsymbol{k}_{\mathrm{T}}$, whereas the longitudinal component $b \cdot P$ is Fourier conjugate to the longitudinal momentum fraction $x = k^+/P^+$. In the present work we restrict to the case $b \cdot P = 0$, thus obtaining only the integral with respect to x of the correlator $\Phi^{[\Gamma]}$ and all TMDs derived from it. It is, however, important to note that lattice calculations can be extended to scan the $b \cdot P$-dependence[2] and obtain, after Fourier transformation, the x-dependence of $\Phi^{[\Gamma]}$ and the TMDs under consideration. Studies of the $b \cdot P$-dependence in the case of straight gauge links ($\eta v = 0$) were carried out in Refs. [7,8], and a related project to obtain the x-dependence of parton distribution functions (PDFs) has been developed in Refs. [18–26].

At leading twist, Eq. (4) defines eight TMDs as coefficient functions with the parametrization

$$\Phi^{[\gamma^+]} = f_1 - \frac{\epsilon_{ij}\boldsymbol{k}_i\boldsymbol{S}_j}{m_N} f_{1T}^{\perp} \tag{5}$$

$$\Phi^{[\gamma^+\gamma^5]} = \Lambda g_1 + \frac{\boldsymbol{k}_{\mathrm{T}} \cdot \boldsymbol{S}_{\mathrm{T}}}{m_N} g_{1T} \tag{6}$$

[2]In a practical calculation, the range of accessible $b \cdot P$ is limited by the available b and P, $|b \cdot P| \leq |\boldsymbol{P}|\sqrt{-b^2}$, leading to an increasing systematic uncertainty at small x.

$$\Phi^{[i\sigma^{i+}\gamma^5]} = \boldsymbol{S}_i h_1 + \frac{(2\boldsymbol{k}_i\boldsymbol{k}_j - \boldsymbol{k}_{\mathrm{T}}^2\delta_{ij})\boldsymbol{S}_j}{2m_N^2} h_{1T}^{\perp} + \frac{\Lambda \boldsymbol{k}_i}{m_N} h_{1L}^{\perp} + \frac{\epsilon_{ij}\boldsymbol{k}_j}{m_N} h_1^{\perp} \tag{7}$$

where m_N denotes the mass, Λ the helicity and $\boldsymbol{S}_T$ the transverse spin of the nucleon. On the lattice, we instead calculate directly the position space correlation function given in Eq. (1) using unrenormalized operators, which, analogous to Eqs. (5)–(7), can also be parametrized in terms of Lorentz invariant amplitudes. Specializing to $b^+ = 0$ and $\boldsymbol{v}_{\mathrm{T}} = \boldsymbol{P}_{\mathrm{T}} = 0$, and working again at leading twist, one has

$$\frac{1}{2P^+}\tilde{\Phi}^{[\gamma^+]}_{\mathrm{unsubtr}} = \tilde{A}_{2B} + im_N\epsilon_{ij}\boldsymbol{b}_i\boldsymbol{S}_j\tilde{A}_{12B} \tag{8}$$

$$\frac{1}{2P^+}\tilde{\Phi}^{[\gamma^+\gamma^5]}_{\mathrm{unsubtr}} = -\Lambda\tilde{A}_{6B} + i[(b\cdot P)\Lambda - m_N(\boldsymbol{b}_{\mathrm{T}}\cdot\boldsymbol{S}_{\mathrm{T}})]\tilde{A}_{7B} \tag{9}$$

$$\frac{1}{2P^+}\tilde{\Phi}^{[i\sigma^{i+}\gamma^5]}_{\mathrm{unsubtr}} = im_N\epsilon_{ij}\boldsymbol{b}_j\tilde{A}_{4B} - \boldsymbol{S}_i\tilde{A}_{9B} - im_N\Lambda\boldsymbol{b}_i\tilde{A}_{10B} + m_N[(b\cdot P)\Lambda - m_N(\boldsymbol{b}_{\mathrm{T}}\cdot\boldsymbol{S}_{\mathrm{T}})]\boldsymbol{b}_i\tilde{A}_{11B}. \tag{10}$$

Note that the Lorentz invariant amplitude combinations $\tilde{A}_{iB}$ are suitable linear combinations of the amplitudes one finds in the most general decomposition, in the absence of the aforementioned constraints on b, v and P. The detailed decomposition into the various amplitudes as calculated by us on the lattice is given in Eqs. (16)–(20) of Ref. [9].

Clearly, there are parallels between Eqs. (5)–(7) and Eqs. (8)–(10). Since the left-hand sides are essentially Fourier transforms of one another, the amplitude combinations $\tilde{A}_{iB}$ are related to Fourier-transformed TMDs through the following relations, as explained in detail in Ref. [9]:

$$\tilde{f}_1^{[1](0)} = 2\tilde{A}_{2B}/\mathcal{Z}^f \tag{11}$$

$$\tilde{g}_1^{[1](0)} = -2\tilde{A}_{6B}/\mathcal{Z}^g \tag{12}$$

$$\tilde{g}_{1T}^{[1](1)} = -2\tilde{A}_{7B}/\mathcal{Z}^g \tag{13}$$

$$\tilde{h}_1^{[1](0)} = -2(\tilde{A}_{9B} - (m_N^2 b^2/2)\tilde{A}_{11B})/\mathcal{Z}^h \tag{14}$$

$$\tilde{h}_{1L}^{\perp[1](1)} = -2\tilde{A}_{10B}/\mathcal{Z}^h \tag{15}$$

$$\tilde{h}_{1T}^{\perp[1](2)} = 4\tilde{A}_{11B}/\mathcal{Z}^h \tag{16}$$

$$\tilde{f}_{1T}^{\perp[1](1)} = -2\tilde{A}_{12B}/\mathcal{Z}^f \tag{17}$$

$$\tilde{h}_1^{\perp[1](1)} = 2\tilde{A}_{4B}/\mathcal{Z}^h \tag{18}$$

where the superscript "[1]" indicates that the first Mellin moment with respect to quark momentum fraction x of the Fourier transform of a generic TMD $f(x, \boldsymbol{k}_{\mathrm{T}}^2, \ldots)$ has been taken [16],

$$\tilde{f}^{[m](n)}(\boldsymbol{b}_{\mathrm{T}}^2, \ldots) \equiv n!\left(-\frac{2}{m_N^2}\partial_{\boldsymbol{b}_{\mathrm{T}}^2}\right)^n \int_{-1}^{1} dx x^{m-1} \cdot \int d^2\boldsymbol{k}_{\mathrm{T}} e^{i\boldsymbol{b}_{\mathrm{T}}\cdot\boldsymbol{k}_{\mathrm{T}}} f(x, \boldsymbol{k}_{\mathrm{T}}^2, \ldots). \tag{19}$$

We have introduced three renormalization factors $\mathcal{Z}^{f,g,h}$ in Eqs. (11)–(18) reflecting the tensor structure of the three TMD operators considered. It is important to note that there is a different $\mathcal{Z}^{f,g,h}$ for each staple geometry (soft factor) and separation b. In the generalized Sivers shift, defined in Eq. (21), the two terms, $\tilde{f}_{1T}^{\perp[1](1)}(\boldsymbol{b}_{\mathrm{T}}^2; \ldots)$ and $\tilde{f}_1^{[1](0)}(\boldsymbol{b}_{\mathrm{T}}^2; \ldots)$, are obtained via Eqs. (11) and (17), in conjunction with Eq. (8), from the matrix element of the same operator with the same value of b and η. The two terms $\tilde{A}_{2B}$ and $\tilde{A}_{12B}$ are isolated, cf. Eq. (8), by using different values of $\epsilon_{ij}\boldsymbol{b}_i\boldsymbol{S}_j$. Thus we expect the factor $\mathcal{Z}^f$ to be the same and to cancel in the ratio. For the Boer-Mulders, transversity and worm-gear shifts defined in Eqs. (22), (23), and (24), the renormalization factor, *a priori*, does not cancel in the ratio even if renormalization is multiplicative. Ignoring discretization errors, we would then attribute the difference in results between different fermion formulations to Z_{TMD}. It is at this point that the assumption underlying lattice calculations stated previously, that at sufficiently large b in physical units all the Z_{TMD} become independent of the spin structure of the operator, is important. In that case, the full renormalization factor would again cancel in the ratios constructed for fixed but large b and fixed η, i.e., for the same staple geometry.

Clearly, such full cancellation will not extend to the $b \to 0$ limit in general. As a case in point, consider the ratio of matrix elements of the (isovector) local axial vector and vector currents within any state $|P, S\rangle$,

$$\left.\frac{\langle P,S|\bar{q}\gamma^+\gamma^5 q|P,S\rangle}{\langle P,S|\bar{q}\gamma^+ q|P,S\rangle}\right|_{\mathrm{ren}} = \frac{Z_A}{Z_V}\left.\frac{\langle P,S|\bar{q}\gamma^+\gamma^5 q|P,S\rangle}{\langle P,S|\bar{q}\gamma^+ q|P,S\rangle}\right|_{\mathrm{bare}}. \tag{20}$$

This ratio is related to, though not identical to, the $b \to 0$ limit of the ratio in Eq. (24); while the denominator of Eq. (24) indeed reduces to the vector current for $b \to 0$, the numerator corresponds to a higher $\boldsymbol{k}_{\mathrm{T}}$-moment of the nonlocal axial vector operator. Nonetheless, if discrepancies between different fermion discretizations arise for Eq. (20), then they must also be countenanced for the $b \to 0$ limit of Eq. (24). Indeed, chiral symmetry implies $Z_A = Z_V$, such that the renormalization factors in Eq. (20) cancel in lattice QCD as long as one uses a (to a good approximation) chirally symmetric discretization; two examples are domain-wall and overlap fermions. However, they

do not cancel for clover fermions; for the clover ensemble considered here, $Z_A/Z_V = 1.096(22)$ [27]. A discrepancy between the unrenormalized ratios obtained in the two fermion discretization schemes thus arises, over and above that expected from finite lattice spacing effects alone. Evidence of such a difference in the worm-gear ratio defined in Eq. (24) at small $\boldsymbol{b}_{\mathrm{T}}$ is discussed in Sec. IV D. In the cases of the generalized Boer-Mulders shift and the tensor charge, chiral symmetry arguments do not constrain the ratio Z_T/Z_V of a local tensor to vector operator, and this ratio can be significantly different for DWF versus clover fermions at finite lattice spacing a. Thus the ratio $\mathcal{Z}^h/\mathcal{Z}^f$ need not cancel and the results can be b-dependent at small b.

Expanding upon a point mentioned above, the $b = 0$ limit of the TMD operator contains additional divergences, which in general also depend on the order of the $\boldsymbol{b}_{\mathrm{T}}$-derivative being taken, i.e., on which $\boldsymbol{k}_{\mathrm{T}}$-moment is considered. In the case of higher $\boldsymbol{k}_{\mathrm{T}}$-moments, the TMD operator does not reduce to a local operator in the $b \to 0$ limit, but becomes a Qiu-Sterman type quark-gluon-quark operator. In general, different renormalization factors could arise depending on which $\boldsymbol{k}_{\mathrm{T}}$-moment is being considered; i.e., the renormalization factors in Eqs. (12) and (13), or within the group of relations Eqs. (14), (15), (16) and (18), need not be the same for $b \to 0$.

Finally, whereas the above discussion is premised on a multiplicative renormalization pattern, it is not guaranteed that such a pattern continues to hold when continuum symmetries, such as rotational symmetry and chiral symmetry, are broken by the lattice formulation. Absence of these symmetries often gives rise to operator mixing, under which the numerators and denominators of the TMD ratios considered here become sums of several terms, destroying multiplicativity and the cancellation of renormalization factors in the ratios. An example of such mixing, at one loop in lattice perturbation theory, for bilocal operators separated by a straight-link path has recently been reported in Ref. [28].

The numerical data discussed in Sec. IV below yield a varied picture with respect to these diverse possibilities, including close agreement, within the present level of statistical accuracy, between the two lattice ensembles for the three ratios, Eqs. (21), (22) and (23), even at small b. On the other hand, at short b, significant differences exist in the ratio defining the generalized g_{1T} worm-gear shift in the TMD limit $|\eta| \to \infty$, Eq. (24). Surprisingly, as discussed in Sec. IV E, these differences persist even at large b for the straight-link path, i.e., in the case $\eta = 0$. As discussed in Sec. IV E, it is very likely that the observed effect is due to the mixing reported in Ref. [28] between the axial and tensor operators that are used to calculate the generalized worm-gear shift and the transversity. While the straight-link case is not directly relevant for TMD observables, it bears on operators used in studies of PDFs [18–26] and challenges our understanding of the renormalization of quark bilocal operators.

III. LATTICE CALCULATIONAL SCHEME

In order to utilize lattice QCD techniques for the evaluation of the fundamental correlator, Eq. (1), it is necessary to boost the problem to a Lorentz frame in which the vectors b and v in Eq. (1) are purely spatial; Minkowski temporal separations cannot be accommodated in the Euclidean lattice setup. For this reason, it is crucial to employ a definition of TMDs in which all separations are spacelike; cf. the discussion in conjunction with Eq. (2) above. With both b and v spacelike, there is no obstacle to the aforementioned boost. In addition, the decomposition given in Eqs. (8)–(10) of the correlator into the invariant amplitudes $\tilde{A}_{iB}$ facilitates translating the obtained data back into the original Lorentz frame; i.e., results for observables cast in terms of these amplitudes in the boosted frame are immediately valid also in the latter.

The lattice parameters of the Wilson-clover and domain-wall fermion (DWF) ensembles analyzed in this work are summarized in Table I. The two ensembles have roughly the same pion mass, about 300 MeV, but differ in the lattice spacing. In contrast to the previous study presented in Ref. [9], we use unitary combinations of sea and valence quarks; i.e., we use the same fermion discretization scheme for the sea and valence quarks and the same values of the sea and valence quark masses.

For the calculation of the quark propagators, we used Wuppertal smeared sources. The smearing parameters were $\{\sigma = 7.284, N = 84\}$ for the DWF ensemble and $\{\sigma = 4.70, N = 35\}$ for the clover ensemble using the conventions given in [30]. In both cases, the gauge configurations were smoothed using 25 iterations of APE smearing with the staples added to the straight link with weight 0.35.

To describe the SIDIS and DY processes, we vary the nucleon three-momentum $\boldsymbol{P}$, the separation $\boldsymbol{b}$, the staple direction $\boldsymbol{v}$ and the corresponding length η of the staple as specified for both the clover and the DWF ensemble in

TABLE I. Lattice parameters of the $n_f = 2 + 1$ flavor domain-wall ensemble generated by the RBC/UKQCD Collaboration and the clover ensemble generated by the JLab/W&M Collaboration. The lattice spacings a and pion masses m_π for the clover and the DWF ensembles are quoted from Refs. [29,30], respectively. Note that a different estimate of $a = 0.127(1)$ fm is reported in [27] for the clover ensemble, set using the Wilson flow parameter w_0, indicating that discretization errors are significant on these coarse lattices.

ID	Clover	DWF
Fermion type	Clover	Domain wall
Geometry	$32^3 \times 96$	$32^3 \times 64$
a (fm)	0.11403(77)	0.0840(14)
m_π (MeV)	317(2)(2)	297(5)
m_N (MeV)	1077(8)	1119(20)
Number of configurations	967	533
Number of measurements	23208	4264

TABLE II. The parameters of the staple-shaped gauge connection, characterized by $\boldsymbol{b}$ and $\eta\boldsymbol{\nu}$, and the nucleon momenta $\boldsymbol{P}$ simulated in both the clover and the domain-wall fermion calculations. L is the spatial size of the lattice and for each n, the range of integers n' is chosen to be large enough to cover the values for which one obtains a useful signal in the three-point correlation functions. For example, in the clover fermion zero momentum case, $n'_{\max}$ is 15 for $|\boldsymbol{b}_{\mathrm{T}}| = 0.11$ fm, 12 for $|\boldsymbol{b}_{\mathrm{T}}| = 0.23$ fm, 11 for $|\boldsymbol{b}_{\mathrm{T}}| = 0.34$ fm and 10 for $|\boldsymbol{b}_{\mathrm{T}}| = 0.45$ fm. In the case of off-axis Wilson lines, the TMD operator was improved by averaging over lattice paths approximating the continuum one; e.g., for $\boldsymbol{b} = 2(\mathbf{e}_2 + \mathbf{e}_3)$, where $\mathbf{e}_i$ denotes the lattice link vector in the i-direction, data were generated for both the sequence of links $(\mathbf{e}_2, \mathbf{e}_3, \mathbf{e}_2, \mathbf{e}_3)$ and the sequence of links $(\mathbf{e}_3, \mathbf{e}_2, \mathbf{e}_3, \mathbf{e}_2)$.

$\boldsymbol{b}/a$	$\eta\boldsymbol{\nu}/a$	$\boldsymbol{P}\cdot aL/(2\pi)$	$\hat{\zeta}_{\mathrm{DWF}}$	$\hat{\zeta}_{\mathrm{clover}}$
$n\cdot(0,0,1)$	$\pm n'\cdot(1,0,0)$	(0,0,0)	0	0
		$(-1,0,0)$	0.412	0.315
$n=-7,\ldots,7$ (clover)	$\pm n'\cdot(1,1,0)$	$(-1,0,0)$	0.292	0.223
$n=-9,\ldots,9$ (DWF)	$\pm n'\cdot(1,-1,0)$		0.292	0.223
$n\cdot(0,1,0)$	$\pm n'\cdot(1,0,0)$	(0,0,0)	0	0
		$(-1,0,0)$	0.412	0.315
$n=-7,\ldots,7$ (clover)	$\pm n'\cdot(0,0,1)$	$(-1,0,0)$	0	0
$n=-9,\ldots,9$ (DWF)	$\pm n'\cdot(1,0,1)$		0.292	0.223
	$\pm n'\cdot(1,0,-1)$		0.292	0.223
$n\cdot(0,1,1)$	$\pm n'\cdot(1,0,0)$	$(-1,0,0)$	0.412	0.315
$n=-4,\ldots,4$				
$n\cdot(0,1,-1)$	$\pm n'\cdot(1,0,0)$	$(-1,0,0)$	0.412	0.315
$n=-4,\ldots,4$				

Table II. The resulting maximum magnitude of the Collins-Soper parameter $\hat{\zeta}$ in this study is $|\hat{\zeta}| = 0.32$ for the clover ensemble and $|\hat{\zeta}| = 0.41$ for the DWF ensemble.

In this study, we work in the isospin symmetric limit and calculate matrix elements of only the isovector combination $(u-d)$ of operators. In this combination, the contributions of the disconnected quark loop diagrams cancel.

IV. NUMERICAL RESULTS

Results for four TMD observables are presented in this section: the T-odd Sivers and Boer-Mulders shifts, as well as the T-even generalized transversity and worm-gear shift associated with the worm-gear TMD g_{1T}. A more detailed description and physical interpretation of these observables is given in Ref. [9].

A. The generalized Sivers shift

The generalized Sivers shift addresses the distribution of transverse momentum of unpolarized quarks in a transversely polarized nucleon, where the transverse momentum direction and the nucleon polarization direction are orthogonal to each other. It is defined by

$$\langle \boldsymbol{k}_y \rangle_{TU}(\boldsymbol{b}_{\mathrm{T}}^2;\ldots) \equiv m_N \frac{\tilde{f}_{1T}^{\perp[1](1)}(\boldsymbol{b}_{\mathrm{T}}^2;\ldots)}{\tilde{f}_1^{[1](0)}(\boldsymbol{b}_{\mathrm{T}}^2;\ldots)}, \tag{21}$$

where m_N is the nucleon mass, $f_{1T}^{\perp}$ is the Sivers TMD [1], and f_1 is the unpolarized TMD. In constructing this ratio, we use unrenormalized operators; cf. Eqs. (8), (11) and (17). Our assumption of the cancellation of the renormalization factors is discussed in Sec. II.

The dependence of the generalized Sivers shift on $\eta|\boldsymbol{\nu}|$ is shown in Fig. 2. In order to describe the SIDIS or the DY process, the length of the staple $|\eta||\boldsymbol{\nu}|$ connecting the quark bilocal operator needs to be extrapolated to infinity. In our setup, the DY process is obtained in the limit $\eta|\boldsymbol{\nu}| \to -\infty$, and SIDIS in the limit $\eta|\boldsymbol{\nu}| \to \infty$.

The data in Fig. 2 indicate the onset of a plateau for $|\eta||\boldsymbol{\nu}| \geq 6a$. A more stringent estimate of the plateau value is obtained in the clover case that has roughly a factor of six larger statistics. Exploiting the evident T-odd behavior, we appropriately average the data for $\pm|\eta||\boldsymbol{\nu}|$ and fit them to a constant for $|\eta||\boldsymbol{\nu}| \geq 6a$ with an upper cutoff of $|\eta| = 10$ for the DWF and $|\eta| = 12$ for the clover data, beyond which the data are noisy. The choice $|\eta||\boldsymbol{\nu}| \geq 6a$ is based on the observation that the results of fits starting at $|\eta||\boldsymbol{\nu}| = 5a, 6a$ and $7a$ are consistent within 1σ. For the error estimate, we quote the jackknife error and ignore the smaller systematic uncertainty associated with the change in the estimate on starting with $|\eta| = 5$ or $|\eta| = 7$ since this paper is not attempting to provide precision estimates. Also, in the constant fit, we do not weight the data by the statistical errors since the points at smaller $|\eta||\boldsymbol{\nu}|$ have smaller statistical errors but larger unquantified systematic errors.

These fits give the magnitude of the results for both DY and SIDIS processes and the sign is taken from the data shown in Fig. 2. The error estimates are obtained using a jackknife method. We find that the statistical uncertainties in the data increase with both $\eta|\boldsymbol{\nu}|$ and $|\boldsymbol{b}_{\mathrm{T}}|$.

The dependence of the generalized Sivers shift on $|\boldsymbol{b}_{\mathrm{T}}|$ in the SIDIS limit is compared for the two different ensembles in Fig. 3 and the dependence on $\hat{\zeta}$ in Fig. 4. The small $|\boldsymbol{b}_{\mathrm{T}}|$

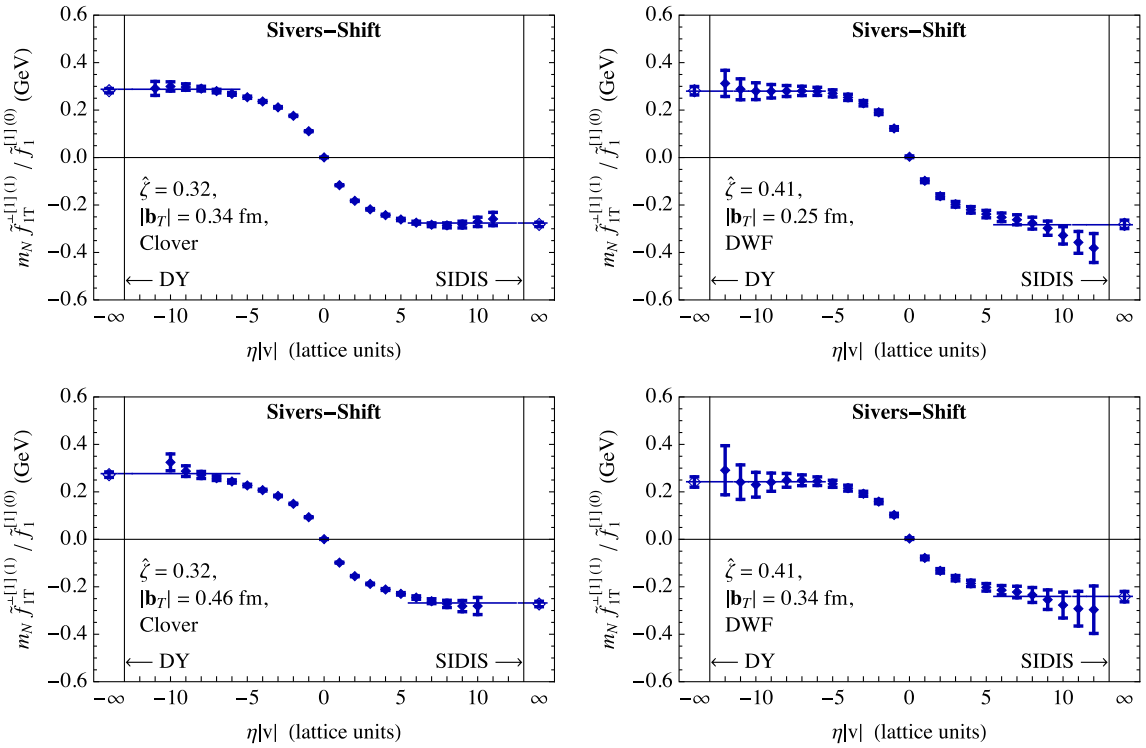

FIG. 2. Dependence of the generalized Sivers shift on the staple extent $\eta|\boldsymbol{v}|$ for the clover (left) and the DWF (right) ensembles at $|\boldsymbol{b}_T| = 3a$ (top) and $4a$ (bottom). The Collins-Soper parameter is fixed at the highest value for which data are available, $\hat{\zeta} = 0.41$ and 0.32 for the DWF and the clover ensembles, respectively. The line shows the central value obtained using a constant fit to the $\pm\eta|\boldsymbol{v}|$ data analyzed separately. The asymptotic estimate (shown using the diamond symbol in the margins on the left and right) is obtained by averaging the $\pm\eta|\boldsymbol{v}|$ fit results and the error is obtained by a jackknife procedure.

region, $|\boldsymbol{b}_T| \leq 3a_{\mathrm{DWF}} \approx 0.25$ fm, in which lattice artifacts and incomplete cancellation of renormalization factors could be expected, is highlighted by the shaded region in Fig. 3, and also in Figs. 6, 9, 12, and 14 for the other TMD observables. For larger $|\boldsymbol{b}_T|$, the data in the SIDIS and DY limit from the clover and the DWF ensembles are consistent for all four TMDs analyzed in this work, suggesting that the fermion discretization scheme and the lattice spacing effects are small. An exception to this pattern is found, however, for the straight-link case, $\eta = 0$, discussed in Sec. IV E.

The data for the Sivers shift in Fig. 3, and also the Boer-Mulders shift in Fig. 6, start to show about 2σ deviation between the two ensembles for $|\boldsymbol{b}_T| > 0.6$ fm. At this separation, the statistical errors in the DWF data are large and we ascribe these deviations to statistical fluctuations; it should be noted that, at these separations, contractions at large $|\eta|$, which cease to provide a useful signal, are not

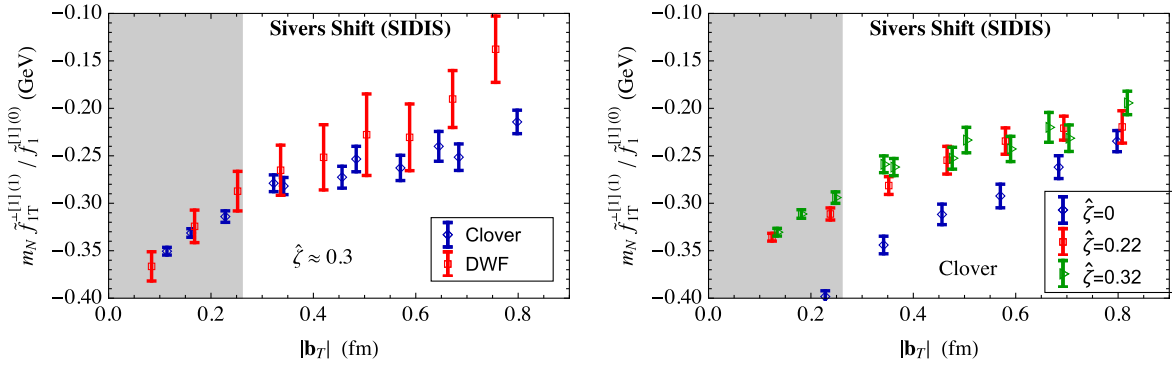

FIG. 3. Dependence of the generalized Sivers shift on $|\boldsymbol{b}_T|$. In the left panel we compare DWF and clover results for $\hat{\zeta} \approx 0.3$ and in the right panel we show the higher precision clover data for three values of $\hat{\zeta}$. The shaded area, $|\boldsymbol{b}_T| \leq 3a_{\mathrm{DWF}} \approx 0.25$ fm, marks the region in which discretization effects could be expected.

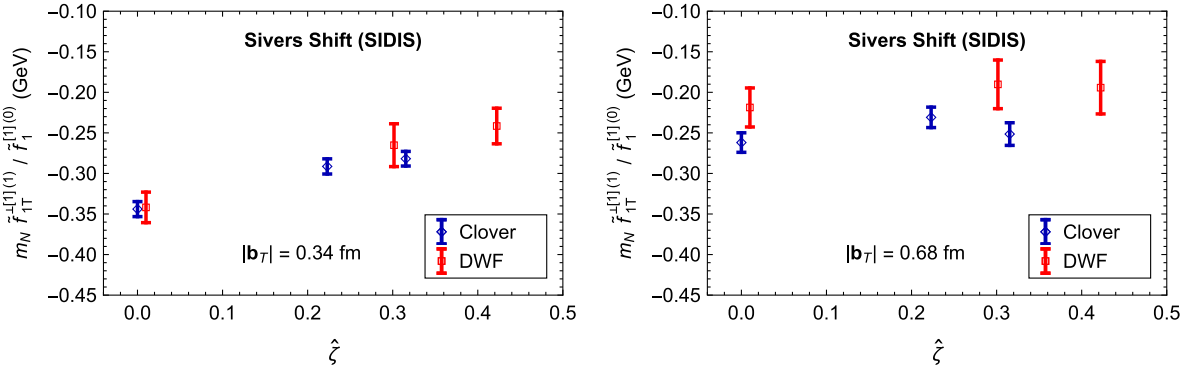

FIG. 4. Dependence of the generalized Sivers shift on $\hat{\zeta}$ for the two different ensembles and for two values of $|\boldsymbol{b}_T| = 0.34$ fm (left) and 0.68 fm (right).

evaluated and therefore do not enter the plateau fits. This may also lead to an underestimate of the uncertainty of the plateau value. On the other hand, for the Sivers shift as well as the Boer-Mulders shift discussed in Sec. IV B, the agreement between the DWF and clover data persists into the region of small $|\boldsymbol{b}_T|$. Our conclusion is that, within errors, no significant differences are seen between data from the two ensembles for these two T-odd TMD observables, even in the limit of small $\boldsymbol{b}_T$.

In Fig. 4, we show the dependence of the generalized Sivers shift on the Collins-Soper evolution parameter $\hat{\zeta}$ for fixed $|\boldsymbol{b}_T| = 0.34$ and 0.68 fm. The data from the two ensembles are consistent, with the data for $|\boldsymbol{b}_T| = 0.68$ fm showing less dependence on $\hat{\zeta}$. Since we have estimates only up to $\hat{\zeta} = 0.41$, a future goal is to extend the calculation of the TMD observables to large enough $\hat{\zeta}$, from where they can be evolved to the light-cone limit, $\hat{\zeta} \to \infty$, using perturbation theory [12].

In Sec. V, we compare these lattice estimates for the generalized Sivers shift with one extracted from experimental data at $\hat{\zeta} = 0.83$. While the trend in the lattice data with $\hat{\zeta} < 0.4$ suggests agreement at $\hat{\zeta} \sim 0.8$, we consider it important to obtain data for $0.4 < \hat{\zeta} < 0.8$ to establish this connection. To increase $\hat{\zeta}$, however, requires simulations with larger nucleon momenta. A recently developed method [17] that controls the rapid growth in statistical errors with momenta [9] is under investigation.

B. The generalized Boer-Mulders shift

The second T-odd TMD observable we evaluate is the generalized Boer-Mulders shift defined by

$$\langle \boldsymbol{k}_y \rangle_{UT}(\boldsymbol{b}_T^2; \ldots) \equiv m_N \frac{\tilde{h}_1^{\perp[1](1)}(\boldsymbol{b}_T^2; \ldots)}{\tilde{f}_1^{[1](0)}(\boldsymbol{b}_T^2; \ldots)}. \tag{22}$$

The Boer-Mulders function $h_1^\perp$ [2] describes the distribution of the transverse momentum of transversely polarized quarks in an unpolarized hadron, where the quark transverse momentum and polarization are orthogonal to one another.

The dependence of the generalized Boer-Mulders shift on $\eta|\boldsymbol{v}|$ is shown in Fig. 5. The data show a plateau at earlier $|\eta||\boldsymbol{v}|$ as compared to the Sivers shift; nevertheless, to preserve uniformity we again extrapolate to the DY and SIDIS limits using a constant fit to data with $|\eta||\boldsymbol{v}| \geq 6a$. Again these results are consistent with those obtained with $|\eta||\boldsymbol{v}| \geq 5a$ or $7a$.

The comparison of the dependence of the Boer-Mulders shift on $|\boldsymbol{b}_T|$ and $\hat{\zeta}$ between the clover and the DWF ensembles is shown in Figs. 6 and 7. We again find that the results are compatible within their statistical uncertainty over the entire range of $|\boldsymbol{b}_T|$; no dependence on the lattice action is observed even in the limit of small $|\boldsymbol{b}_T|$. In Ref. [16], the dependence of the generalized Boer-Mulders shift on $\hat{\zeta}$ for pions was studied up to $\hat{\zeta} = 2.03$ by taking advantage of the lighter mass and better signal-to-noise ratio in pion correlation functions as compared to those for nucleons. Results for the pion show that a significant portion of the evolution to large $\hat{\zeta}$ is already achieved when $\hat{\zeta} \sim 2$.

The higher statistics clover data in the right panels of Figs. 3 and 6 show that the two T-odd TMD observables of the nucleon, the Sivers and the Boer-Mulders shifts (SIDIS case), increase with $\hat{\zeta}$ and $|\boldsymbol{b}_T|$, and the data at the three values of $\hat{\zeta}$ have, within 1σ errors, converged by $|\boldsymbol{b}_T| \approx 0.8$ fm.

C. The transversity h_1

The T-even TMDs, unlike the T-odd TMDs such as the Sivers and Boer-Mulders distributions, are process independent, i.e., the same for DY and SIDIS processes. They were initially studied in lattice QCD in a truncated fashion by using a straight Wilson line [7,8] and the treatment was subsequently extended to the physically relevant case of staple-shaped paths describing the SIDIS and DY processes. It has been observed that the difference between the two approaches is in many cases small for T-even TMDs

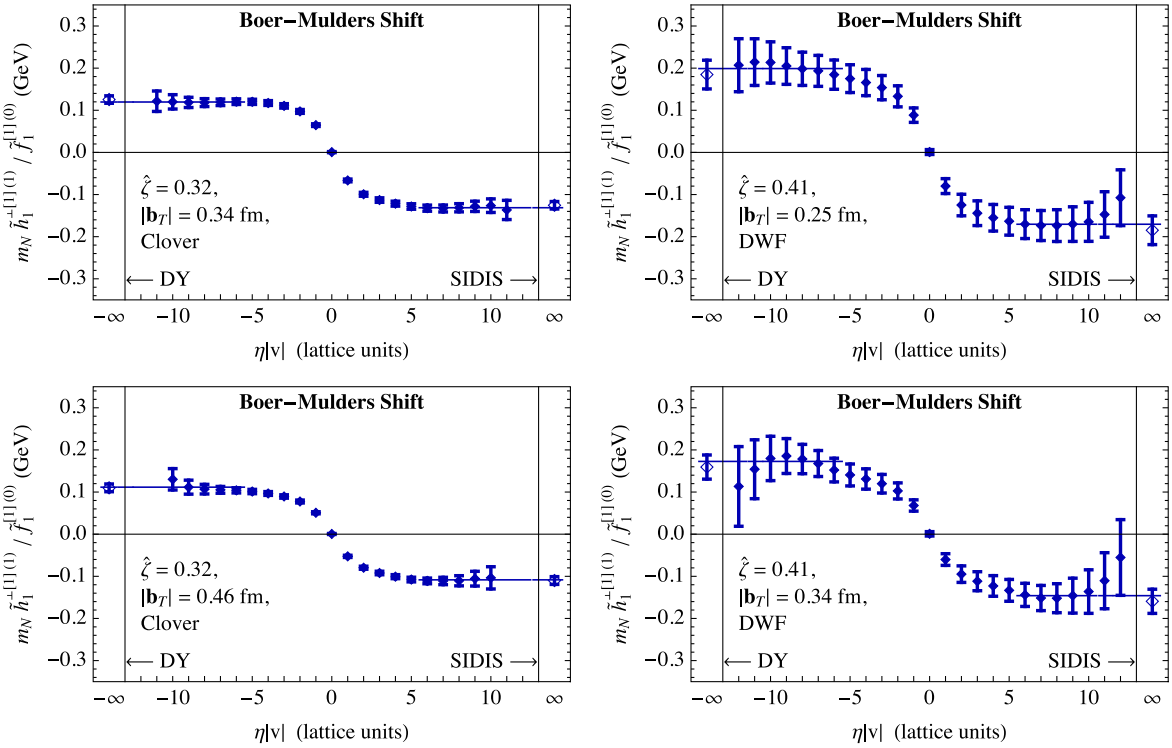

FIG. 5. Dependence of the generalized Boer-Mulders shift on the staple extent $\eta|\boldsymbol{v}|$ for the clover (left) and the DWF (right) ensembles. The rest is the same as in Fig. 2.

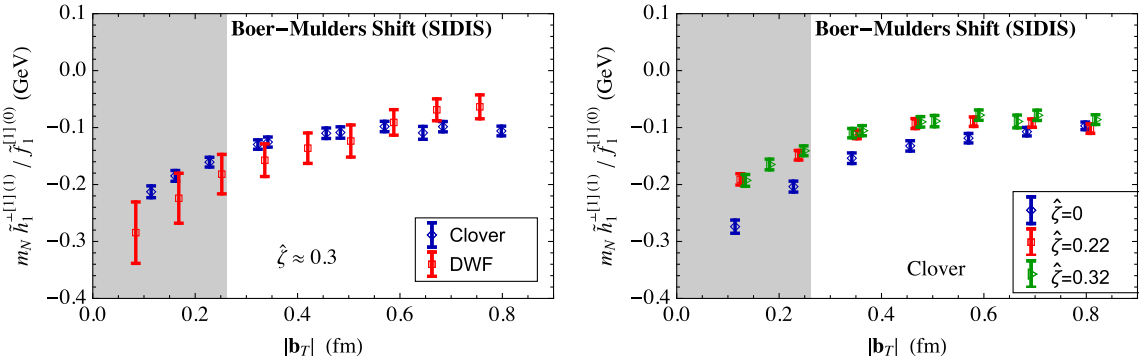

FIG. 6. Dependence of the generalized Boer-Mulders shift on $|\boldsymbol{b}_\mathrm{T}|$ for the two ensembles (left), and for three different values of $\hat{\zeta}$ analyzed on the clover ensemble (right). The rest is the same as in Fig. 3.

[9]; i.e., there is only a mild η-dependence. In this study, our observations are similar for the two different lattice discretization schemes, and at the lighter pion masses investigated, although the picture for the g_{1T} worm-gear shift discussed in Secs. IV D and IV E is not as clear cut.

The first T-even observable we present is the generalized tensor charge defined by the ratio between the transversity and the unpolarized function:

$$\frac{\tilde{h}_1^{[1](0)}(\boldsymbol{b}_\mathrm{T}^2;\ldots)}{\tilde{f}_1^{[1](0)}(\boldsymbol{b}_\mathrm{T}^2;\ldots)}. \tag{23}$$

It is called the generalized tensor charge because the integral of the transversity, obtained in position space by setting $\boldsymbol{b}_\mathrm{T}^2 = 0$, formally gives the nucleon tensor charge: $g_T^{u-d} = \int dx d^2\boldsymbol{k}_\mathrm{T} h_1(x, \boldsymbol{k}_\mathrm{T}^2) = \tilde{h}_1^{[1](0)}(\boldsymbol{b}_\mathrm{T}^2 = 0)$.

The data for the transversity ratio given in Fig. 8 show that the $\eta|\boldsymbol{v}|$-dependence is much smaller than for the T-odd TMDs but nonzero. The DWF data are noisy and do not show a clear plateau. The higher statistics clover data, and a previous study using a mixed-action DWF-on-AsqTad lattice scheme at $m_\pi = 518$ MeV with $\hat{\zeta} = 0.39$ [9], show a plateau from which the asymptotic value can be extracted. We again fit the data with $|\eta||\boldsymbol{v}| \geq 6a$ to a constant for both

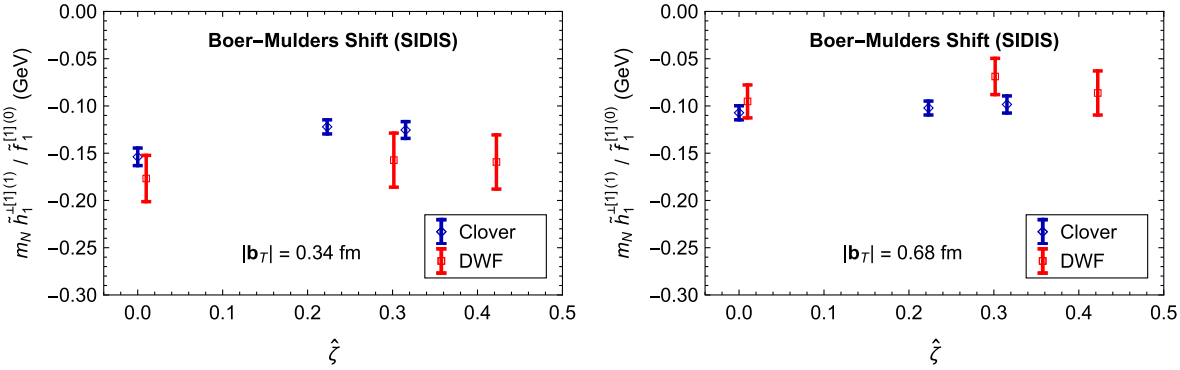

FIG. 7. Dependence of the generalized Boer-Mulders shift on $\hat{\zeta}$ for two values of $|\boldsymbol{b}_{\mathrm{T}}| = 0.34$ fm (left) and 0.68 fm (right).

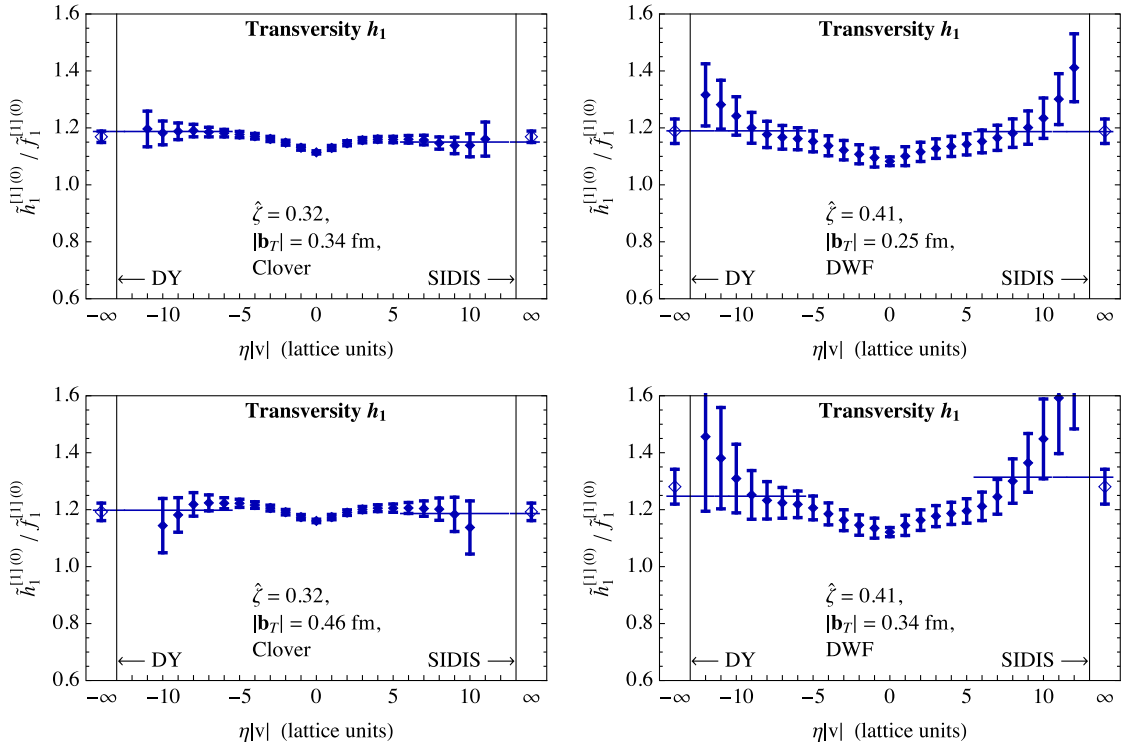

FIG. 8. Dependence of the transversity ratio $\tilde{h}_1^{[1](0)}/\tilde{f}_1^{[1](0)}$ on the staple extent $\eta|\boldsymbol{v}|$ for the clover (left) and the DWF (right) ensembles. The rest is the same as in Fig. 2.

ensembles. The $|\boldsymbol{b}_{\mathrm{T}}|$ and $\hat{\zeta}$ dependences of the transversity ratio are illustrated in Figs. 9 and 10. The data in the left panel of Fig. 9 for both ensembles show a consistent plateau for $|\boldsymbol{b}_{\mathrm{T}}| > 0.3$ fm. Again, as in the case of the T-odd TMDs, the DWF and the clover data agree even in the regime of small $|\boldsymbol{b}_{\mathrm{T}}|$. Also, the data in Fig. 10 show no significant dependence on $\hat{\zeta}$.

D. The generalized g_{1T} worm-gear shift

The second T-even TMD observable considered in this work is the generalized worm-gear shift defined by

$$\langle k_x \rangle_{TL}(\boldsymbol{b}_{\mathrm{T}}^2; \ldots) \equiv m_N \frac{\tilde{g}_{1T}^{[1](1)}(\boldsymbol{b}_{\mathrm{T}}^2; \ldots)}{\tilde{f}_1^{[1](0)}(\boldsymbol{b}_{\mathrm{T}}^2; \ldots)}, \tag{24}$$

where g_{1T} is one of the "worm-gear" functions, the transversal helicity [31]. The dependence of the generalized g_{1T} shift on $\eta|\boldsymbol{v}|$ is shown in Fig. 11. Similar to what is observed in the transversity ratio, the generalized g_{1T} shift on the clover lattices shows little change in the transition from the straight Wilson line ($\eta = 0$) to the staple-shaped path, other than the cusp at $\eta = 0$. The DWF data show a dependence on η, but note that the uncertainties are large. Figure 12 shows the dependence of the SIDIS (or equivalently DY) limits of the generalized g_{1T} shift on $|\boldsymbol{b}_{\mathrm{T}}|$ and $\hat{\zeta}$ for the two different ensembles. Again, the results from the two ensembles are consistent, as expected, for $|\boldsymbol{b}_{\mathrm{T}}| \geq 0.3$ fm.

Both the worm-gear shift (Fig. 13) and the transversity (Fig. 10) show little dependence on $\hat{\zeta}$ in contrast to the data

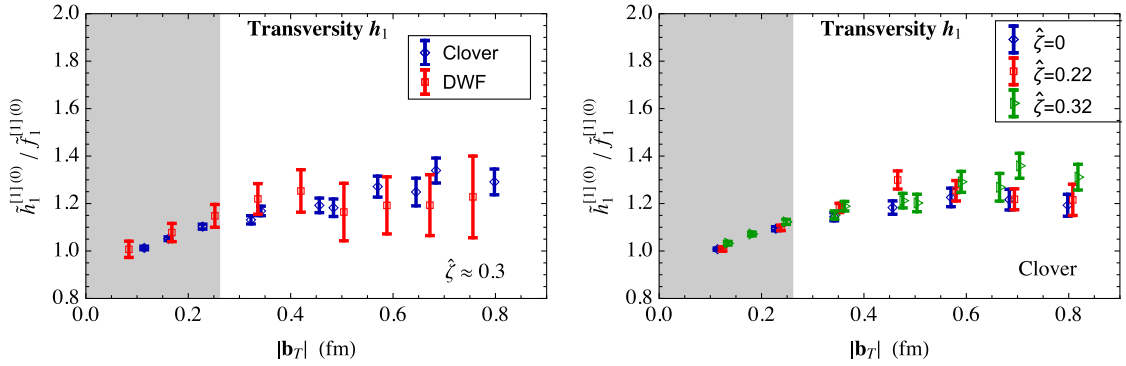

FIG. 9. Dependence of the transversity ratio $\tilde{h}_1^{[1](0)}/\tilde{f}_1^{[1](0)}$ on $|\boldsymbol{b}_T|$ for the two ensembles (left), and for three different values of $\hat{\zeta}$ analyzed on the clover ensemble (right). The rest is the same as in Fig. 3.

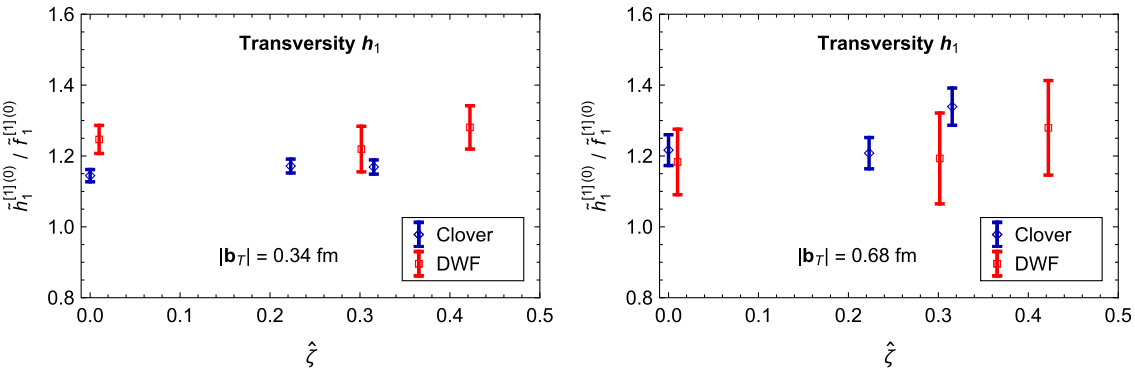

FIG. 10. Dependence of the transversity ratio $\tilde{h}_1^{[1](0)}/\tilde{f}_1^{[1](0)}$ on $\hat{\zeta}$ for two values of $|\boldsymbol{b}_T| = 0.34$ fm (left) and 0.68 fm (right).

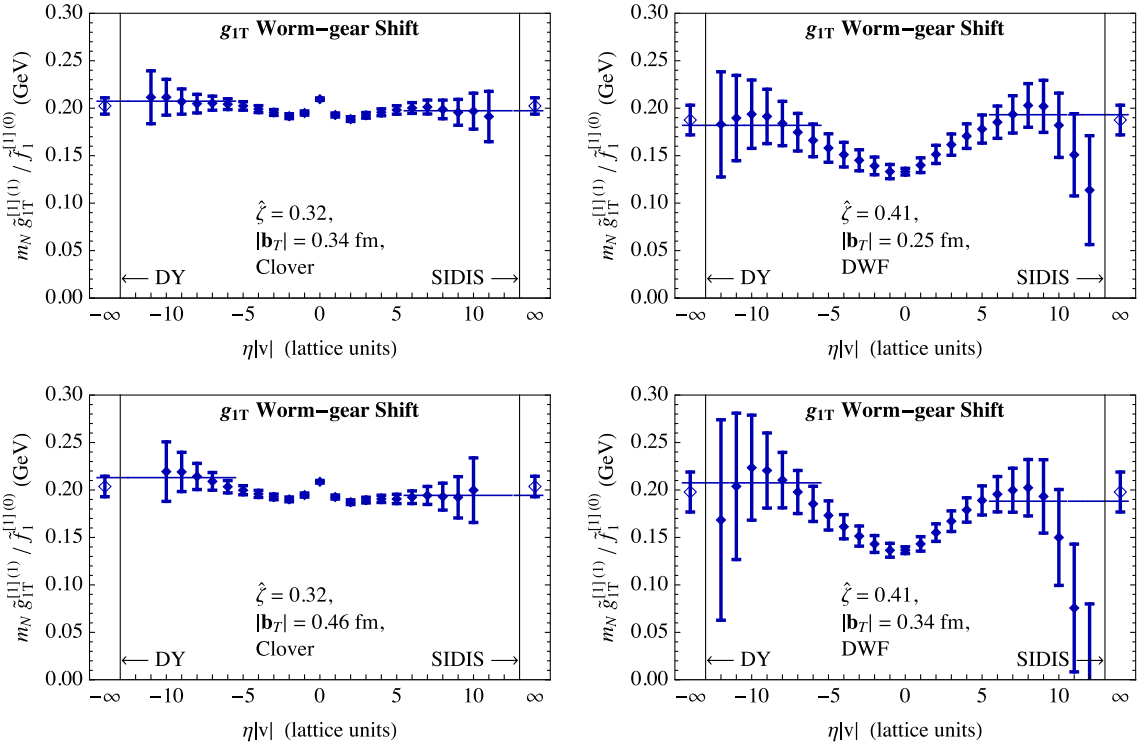

FIG. 11. Dependence of the generalized g_{1T} worm-gear shift on the staple extent $\eta|\boldsymbol{v}|$ for the clover (left) and the DWF (right) ensembles. The rest is the same as in Fig. 2.

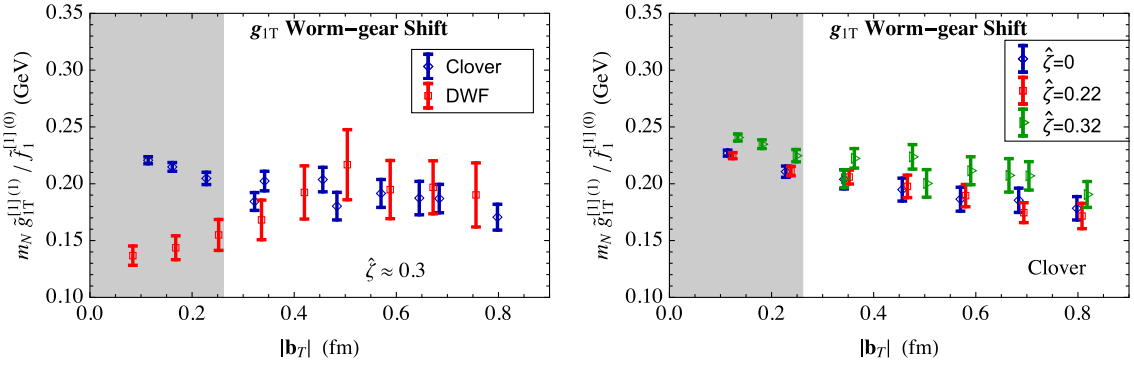

FIG. 12. Dependence of the generalized g_{1T} worm-gear shift on $|\boldsymbol{b}_{\mathrm{T}}|$ for the two ensembles (left), and for three different values of $\hat{\zeta}$ analyzed on the clover ensemble (right). The rest is the same as in Fig. 3.

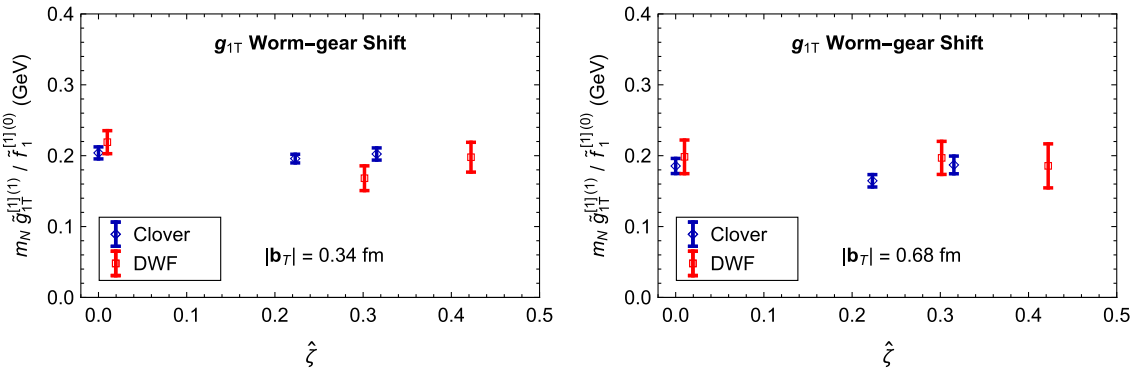

FIG. 13. Dependence of the generalized g_{1T} worm-gear shift on $\hat{\zeta}$ for two values of $|\boldsymbol{b}_{\mathrm{T}}| = 0.34$ fm (left) and 0.68 fm (right).

for the T-odd shifts given in Figs. 3 and 6 which show a significant difference between the $\hat{\zeta} = 0$ and $\hat{\zeta} = 0.22$ or 0.32 cases, especially at small $|\boldsymbol{b}_{\mathrm{T}}|$.

The generalized g_{1T} worm-gear shift does differ qualitatively from the other TMD ratios studied, in that a significant difference between the two ensembles is observed when $|\boldsymbol{b}_{\mathrm{T}}| \leq 0.25$ fm. Further data are needed to clarify whether this difference is due to the failure of the cancellation of renormalization factors in the ratios as discussed in Sec. II or different discretization effects in the two lattice formulations. It is important to bear in mind that for the TMD observable of interest, the generalized g_{1T} worm-gear shift, the two lattice formulations give consistent results for $|\boldsymbol{b}_{\mathrm{T}}| \geq 0.3$ fm as shown in Fig. 12.

Overall, in the SIDIS and DY limit, the data presented exhibit consistency between the two lattice ensembles for all four observables considered once the quark separation $|\boldsymbol{b}_{\mathrm{T}}|$ in the bilocal TMD operator exceeds about three lattice spacings, indicating that, in the regime of finite physical extent, the lattice operators approximate the expected continuum behavior. Only in the case of the generalized g_{1T} worm-gear shift, significant differences between domain-wall and clover fermions are observed at small $|\boldsymbol{b}_{\mathrm{T}}|$. For the other three observables, it is encouraging to note that the agreement persists into the quasilocal regime.

E. Transversity and worm-gear shift from straight gauge link paths

To obtain further insight into the discrepancy between the data, at small $\boldsymbol{b}_{\mathrm{T}}$, from the two lattice formulations in the generalized g_{1T} worm-gear shift and buttressed by the superior statistical accuracy of the data when $\eta = 0$, we examined also the case of a straight gauge connection for the T-even TMD operators. It should be emphasized that this is not the physically relevant case for TMD studies; both the SIDIS and the DY processes are described by a staple-shaped gauge connection with $|\eta| \to \infty$ that encodes final and initial state interactions, respectively. However, such straight-link operators are used, e.g., in the study of PDFs in the approach developed in Refs. [18–26].

The data for the two T-even quantities, the generalized worm-gear shift and the transversity, for straight-link paths connecting the quark fields are shown in Fig. 14 (the corresponding data for the T-odd Sivers and Boer-Mulders shifts are consistent with zero, as expected). The data for the clover and DWF fermions agree for the transversity $\tilde{h}_1^{[1](0)}(\boldsymbol{b}_{\mathrm{T}}^2; \ldots)/\tilde{f}_1^{[1](0)}(\boldsymbol{b}_{\mathrm{T}}^2; \ldots)$ for all values of $\boldsymbol{b}_{\mathrm{T}}$ starting at a separation of one link, even at the improved level of accuracy afforded by the straight-link case. This is consistent with the pattern seen in Fig. 9. However, examining

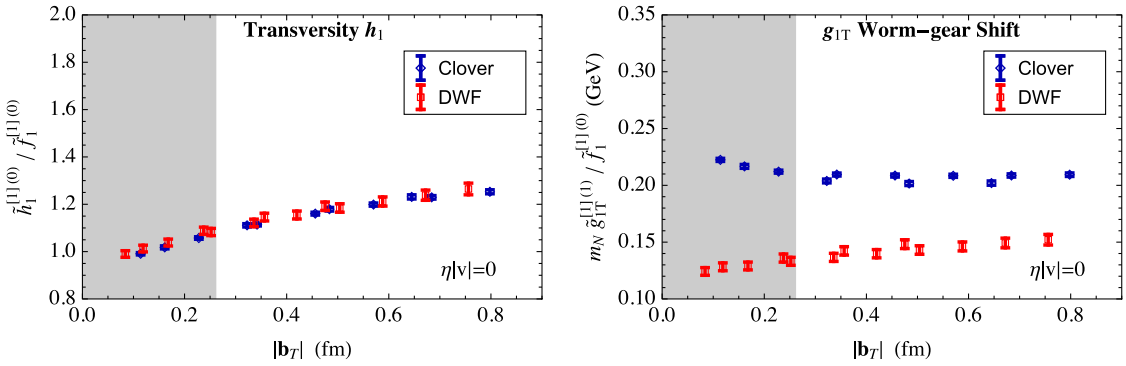

FIG. 14. Dependence of the transversity (left) and generalized g_{1T} worm-gear shift (right) on the length of the straight-link paths, $|\boldsymbol{b}_T|$, for the two different ensembles. The striking observation is that the difference between the DWF and clover data for the worm-gear shift persists for all $|\boldsymbol{b}_T|$. The data shown are for nucleon momentum $|\boldsymbol{P}| = 2\pi/(aL)$; results for $\boldsymbol{P} = 0$ coincide with these data within the uncertainties shown.

the generalized worm-gear shift, $m_N \tilde{g}_{1T}^{[1](1)}(\boldsymbol{b}_T^2; \ldots)/\tilde{f}_1^{[1](0)}(\boldsymbol{b}_T^2; \ldots)$, one is confronted with the surprising result that the data on the two ensembles differ for all $\boldsymbol{b}_T$. The discrepancy observed in the staple-link case at only small $\boldsymbol{b}_T$ with $\eta \to \infty$, cf. Fig. 12, opens up for $\eta = 0$ to persist for all $\boldsymbol{b}_T$ considered. This difference can be traced back to the opposite nature of the cusp in the two data sets (DWF versus clover) at $\eta = 0$ as evident from Fig. 11.

The recent one-loop lattice perturbation theory calculation, presented in Ref. [28], shows that for clover fermions there is a mixing of the straight-link bilocal axial and tensor quark operators that we have used to calculate the generalized worm-gear shift and the transversity. This mixing is a lattice artifact due to the explicit breaking of the chiral symmetry in the clover formulation. To analyze the impact of the mixing on the clover data in detail requires calculating the contributions of all the nonzero Lorentz invariants in the axial (tensor) channel [see Eqs. (19) and (20) in Ref. [9]], which we have not done. In our data, an effect is only seen in the worm-gear shift, but not in the generalized transversity. This would be the expected behavior in a scenario where the worm-gear shift, after taking into account kinematic factors, is much smaller than the generalized transversity. We speculate this to be the reason for the mixing effects being manifest in only the worm-gear shift.

To summarize, our key observation is that a difference between DWF and clover results is observed only in the case where there is a mixing between operators, calculated at one loop in Ref. [28]. Whether the mixing, analyzed at one loop, is the explanation for the full nonperturbative effect seen remains to be confirmed by future calculations.

V. COMPARISON WITH EXPERIMENTAL ESTIMATE OF GENERALIZED SIVERS SHIFT

In this section, we compare the lattice QCD calculation of the generalized Sivers shift defined in Eq. (21) with the result extracted from SIDIS experimental data.

At leading order in perturbation theory [32], the unpolarized function and the Sivers function are written as

$$\tilde{f}_{1,q}^{(0)}(x, b; Q) = f_q(x, Q), \tag{25}$$

$$\tilde{f}_{1T,q}^{\perp(1)}(x, \boldsymbol{b}_T^2; Q, \ldots) = -\frac{1}{2m_N} T_{q,F}(x, x; Q), \tag{26}$$

where $f_q(x, Q)$ is the collinear PDF, and $T_{q,F}(x, x, Q)$ is the twist-3 Qiu-Sterman quark-gluon correlation function. The x-integral of the collinear PDF is the number of valence quarks in a proton, so the denominator of Eq. (21) becomes 1 for the $u - d$ isovector combination. For the Qiu-Sterman function, Ref. [32] uses the ansatz

$$T_{q,F}(x, x, Q; \alpha_q, \beta, N_q) = N_q \frac{(\alpha_q + \beta)^{(\alpha_q+\beta)}}{\alpha_q^{\alpha_q} \beta^{\beta}} x^{\alpha_q}(1 - x)^{\beta} f_q(x, Q), \tag{27}$$

with the parameters N_q, α_q and β determined by a global fit to the Sivers asymmetry data in SIDIS experiments at HERMES, COMPASS and Jefferson Lab. Following Ref. [32], we take the Qiu-Sterman function expressed in terms of fit parameters with errors and ignore the smaller uncertainties in the collinear PDF, given in Ref. [33]. Using these parametrized functions, the error in the generalized Sivers shift is estimated by generating a bootstrap sample for the numerator using a normal distribution with mean and error given in Ref. [32]. We choose the momentum scale $Q = \sqrt{2.4}$ GeV, which is the typical momentum scale of the HERMES experiments, large enough to expect perturbation theory to be reliable (i.e., $Q \gg \Lambda_{\mathrm{QCD}}$), and close to the scale of our lattice calculations ($Q \approx 1/a$). TMDs also depend on the variable ζ, and the authors in Ref. [32] use $\zeta = Q$, which corresponds to $\hat{\zeta} = \zeta/2m_N = 0.83$ in our calculation.

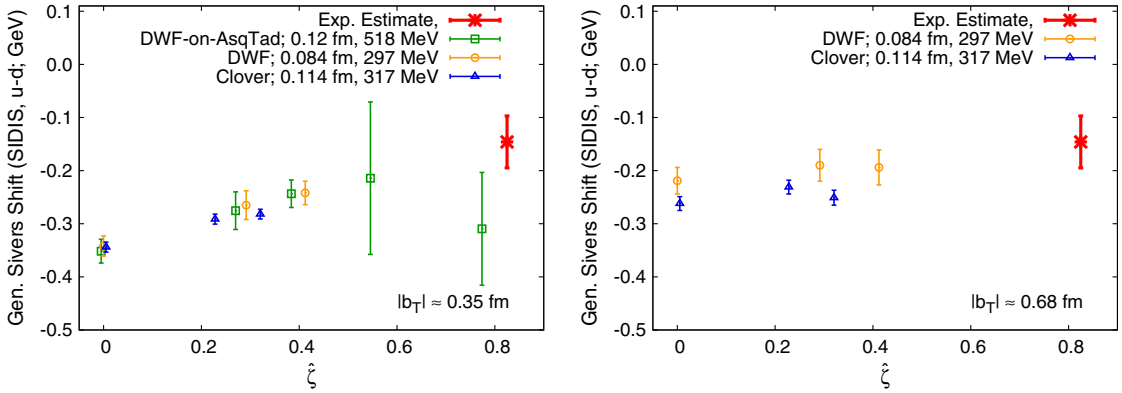

FIG. 15. Experimental extraction of the SIDIS generalized Sivers shift at $\hat{\zeta} = 0.83$, together with lattice QCD data in the SIDIS limit, $\eta \to \infty$, as a function of the Collins-Soper parameter $\hat{\zeta}$. Lattice data for $|\boldsymbol{b}_{\mathrm{T}}| \approx 0.35$ fm are given in the left panel where we have included results from an earlier DWF-on-Asqtad study given in Ref. [9]. Results for $|\boldsymbol{b}_{\mathrm{T}}| \approx 0.68$ fm are given in the right panel.

With these simplifications, the generalized Sivers shift is defined via the x-integrals of the TMDs over the range $[-1, 1]$, with the data at negative values of x given by the antiquark distribution. Note that in the numerator in Eq. (21), the quark and antiquark distributions are summed, whereas in the denominator, the antiquark distribution is subtracted from the quark distribution [31]. The desired phenomenological estimate of the generalized Sivers shift for the isovector operator is then given by

$$\langle \boldsymbol{k}_y \rangle_{TU}^{\mathrm{SIDIS}} = m_N \frac{\tilde{f}_{1T,u}^{\perp[1](1)} - \tilde{f}_{1T,d}^{\perp[1](1)}}{\tilde{f}_{1,u}^{[1](0)} - \tilde{f}_{1,d}^{[1](0)}} = -0.146(49). \quad (28)$$

Note that this ratio, calculated using the leading order expressions given in Eqs. (25) and (26), is independent of $\boldsymbol{b}_{\mathrm{T}}^2$ and the momentum scale. The scale dependence cancels in the ratio at leading order in perturbation theory, and thus, any reasonable choice should have a small impact on the generalized Sivers shift.

In Fig. 15, we compare this result with lattice estimates reproduced from Fig. 4 for two values of $|\boldsymbol{b}_{\mathrm{T}}| \approx 0.35$ and 0.68 fm. In the left panel, we also include previous lattice results from a DWF-on-Asqtad study given in Ref. [9]. Note that the extraction of the experimental estimate has been done at $\hat{\zeta} = 0.83$, while precise lattice results are obtained at $\hat{\zeta} \leq 0.41$ (the earlier lattice data points at $\hat{\zeta} > 0.41$ from Ref. [9] have large uncertainties). We observe the following: First, the three lattice ensembles with different pion masses ($m_\pi = 518$ MeV versus $m_\pi \approx 300$ MeV) and different discretization schemes at different values of the lattice spacing give consistent results. Second, as $|\boldsymbol{b}_{\mathrm{T}}|$ and/or $\hat{\zeta}$ are increased, the lattice results tend toward the phenomenologically extracted value. Third, the observed behavior is similar to that seen in the study using pions in Ref. [16]. Thus, taking the trend in our data between $0.2 < \hat{\zeta} < 0.41$ at face value, it is reasonable to expect future lattice estimates at $\hat{\zeta} \approx 0.8$ to agree with the phenomenological value.

For completeness, we applied similar considerations to the Boer-Mulders shift. To extract the Boer-Mulders distributions, a number of assumptions have to be made since the experimental data are limited [34]. These assumptions have not been validated, and even the sign of the contributions for the various antiquark flavors has not been resolved. Thus, we warn the reader that the accuracy of the following considerations is difficult to assess. One way to obtain an estimate is to use the assumptions given in Ref. [34] and the parametrization of the Sivers distribution given in Ref. [32]. We furthermore assume that relations between antiquark distributions, which are numerically smaller than the corresponding quark distributions, used in Ref. [34] in k_T space carry over unchanged to b_T space in which we have lattice data. With these caveats, our "phenomenological estimate" for the Boer-Mulders shift, also for $\hat{\zeta} = 0.83$, is -0.07. Note that this represents the b_T independent leading order term. Our lattice estimate, given in Fig. 7, is between -0.1 and -0.15.

On the other hand, following Ref. [35], the Boer-Mulders distributions can be parametrized as

$$h_1^{\perp a}(x, k_T^2) = N_a x^{\alpha_a} (1-x)^{\beta_a} e^{-k_T^2/\mu^2} f_1^a(x, k_T^2),$$
$$f_1^a(x, k_T^2) = f_1^a(x) \frac{e^{-k_T^2/\mu^2}}{\pi \langle k_T^2 \rangle}, \quad (29)$$

where a runs over the u and d quark flavors and N_a, α_a, β_a and μ are parameters to be determined from fits to the data. An identical parametrization is made for the antiquark distributions $\bar{h}_1^{\perp a}(x, k_T^2)$ and $\bar{f}_1^a(x, k_T^2)$ with parameters $N_{\bar{a}}$, $\alpha_{\bar{a}}$, $\beta_{\bar{a}}$ and μ. We use the values for the parameters α_a, β_a and μ for both quarks and antiquarks given in Refs. [34,35], again assuming the Boer-Mulders and the Sivers distributions to be the same up to different normalizations N_a and $N_{\bar{a}}$ that are determined from fits to the Boer-Mulders data.

Using the parameter values given there, we carry out the integration over x and k_T with $\langle k_T^2 \rangle = 0.25$ GeV^2 and get -0.68 at $b_T = 0.35$ fm and -0.50 at $b_T = 0.68$ fm. The difference between the two sets of estimates we obtain is due to the difference in the Sivers function in Ref. [32] versus that given in Ref. [34]. Compounding the uncertainty of the analysis is the fact that the experimental data for extracting the Boer-Mulders distributions is insufficient. We, therefore, consider this analysis for the Boer-Mulders shift to be preliminary and do not have a reasonable error estimate.

In the case of transversity, the most straightforward quantity to compare between phenomenological analyses of the experimental data and lattice QCD calculations is the tensor charge. A recent comparison carried out in Ref. [36] shows that the phenomenological values are about 30% smaller than the lattice results. Lastly, we note that, at this point, there is very little experimental data from which to extract the worm-gear shift.

VI. CONCLUSION

We present lattice QCD results for the time-reversal odd generalized Sivers and Boer-Mulders transverse momentum shifts applicable to SIDIS and DY experiments; and for the T-even generalized transversity, related to the tensor charge, and the generalized g_{1T} worm-gear shift. The lattice calculations were performed on two different $n_f = 2 + 1$ flavor ensembles: a DWF ensemble with lattice spacing $a = 0.084$ fm and pion mass 297 MeV, and a clover ensemble with $a = 0.114$ fm and pion mass 317 MeV. The high statistics analysis of the clover ensemble yields estimates with $O(10\%)$ uncertainty for all four quantities over the range $|\boldsymbol{b}_{\mathrm{T}}| < 0.8$ fm and $\hat{\zeta} \lesssim 0.3$. Estimates from the DWF ensemble have appreciably higher statistical errors owing to the more limited statistics, but are expected to have smaller systematic uncertainties.

Our results for TMD observables on two ensembles with comparable pion masses, but with very different discretization of the Dirac action provide an opportunity for an empirical test of the presence of finite lattice spacing effects and the cancellation of renormalization factors in the ratios of correlation functions considered. Estimates with DWF at $a = 0.084$ fm are expected to have small discretization errors. Apart from the notable exception of the generalized g_{1T} worm-gear shift, the consistency of DWF results with those using clover fermions on coarser lattices with $a = 0.114$ fm suggests that lattice discretization effects are small.

In continuum QCD, the nonlocal TMD operator is renormalized multiplicatively with a renormalization factor composed of a product of soft factors, operator specific part, and quark wave function renormalizations. This pattern is, *a priori*, not guaranteed to carry over to the lattice formulation of the theory. Even though all the TMD observables considered in the present work were calculated using unrenormalized operators, the results for the ratios obtained using DW and clover fermions are consistent except in some specific circumstances. To the extent that they are consistent, this can be taken as an indication that the renormalization factors largely cancel in the ratios considered.

The results for the TMD ratios obtained in the SIDIS and DY limits, i.e., using staple-shaped gauge connections, agree within uncertainties for all four observables studied once the quark separation $|\boldsymbol{b}_{\mathrm{T}}|$ in the bilocal TMD operator exceeds about three lattice spacings. The agreement furthermore persists into the regime of small $|\boldsymbol{b}_{\mathrm{T}}|$ for all but one of the TMD observables, namely, the generalized g_{1T} worm-gear shift. Thus, within the statistical accuracy of the calculation, the discretization effects and the cancellation of the renormalization factors in our TMD observables in the SIDIS and DY limits appear under control at finite physical separations $|\boldsymbol{b}_{\mathrm{T}}|$.

A surprising departure from the expectation that renormalization factors generally become independent of the Dirac structure for well-separated bilocal operators is observed for the T-even g_{1T} worm-gear shift in the $\eta = 0$ straight-link case. The discrepancy in the g_{1T} worm-gear shift at small $|\boldsymbol{b}_{\mathrm{T}}|$ for $\eta \to \infty$ is seen to persist to all values of $|\boldsymbol{b}_{\mathrm{T}}|$ for $\eta = 0$. As discussed in Sec. IV E, we provide a plausible explanation based on the recent one-loop perturbative calculation [28] of a mixing, a lattice artifact in the clover formulation, between axial and tensor operators for our choice of the direction of the straight-link path *vis-à-vis* the operator tensor index. Further studies that include a complete analysis of the mixing, including a nonperturbative calculation of the relevant renormalization factors, are warranted to establish our observation. Note that, whereas the T-even functions with $\eta = 0$ are not immediately relevant for TMD applications, which call for staple-shaped gauge connections, such operator mixing would need to be taken into account in the study of PDFs [18–26], which employ straight gauge connections.

Compiling the lattice TMD results obtained to date, as exhibited in Fig. 15 for the case of the Sivers shift, we observe that three lattice ensembles with different pion masses and different discretization effects give consistent results. In an ideal case, in which estimates are obtained with arbitrarily small errors, such a consistency could be taken as evidence that the dependence on the light quark masses and the discretization corrections are both small. Furthermore, as discussed in Sec. II, the renormalization factors cancel in the ratio defining the Sivers shift. We therefore regard it as reasonable to compare lattice results obtained to date for the Sivers shift at pion masses down to $m_\pi \approx 300$ MeV to a phenomenological estimate extracted from experimental data. Indications of consistency with the experimental result at $\hat{\zeta} \gtrsim 0.8$ (cf. Fig. 15) suggest that, within our uncertainties, lattice artifacts for several

moments of TMDs are already reasonably small at the values of the lattice parameters employed. Thus, future higher precision calculations on ensembles with lighter quark masses and smaller lattice spacings and incorporating improvements such as momentum smearing are well motivated.

ACKNOWLEDGMENTS

We thank Martha Constantinou, Zhongbo Kang, Stefan Meinel, Duff Neill and Ivan Vitev for fruitful discussions. The RBC/UKQCD Collaboration is gratefully acknowledged for providing the DWF ensemble analyzed in this work, as are R. Edwards, B. Joó, and K. Orginos for providing the clover ensemble, which was generated using resources provided by XSEDE (supported by National Science Foundation Grant No. ACI-1053575). Computations were performed using resources provided by the U.S. DOE Office of Science through the National Energy Research Scientific Computing Center (NERSC), a DOE Office of Science User Facility, under Contract No. DE-AC02-05CH11231, as well as through facilities of the USQCD Collaboration, employing the Chroma software suite [37]. The work of T. Bhattacharya, R. Gupta and B. Yoon is supported by the U.S. Department of Energy, Office of Science, Office of High Energy Physics under Contract No. DE-KA-1401020 and the LANL LDRD program. M. Engelhardt, J. Negele and A. Pochinsky are supported by the U.S. Department of Energy, Office of Science, Office of Nuclear Physics through Grants No. DE-FG02-96ER40965, No. DE-SC-0011090 and No. DE-FC02-06ER41444 respectively. S. Syritsyn was supported by the U.S. Department of Energy, Office of Science, Office of Nuclear Physics under Contract No. DE-AC05-06OR23177 and by the RIKEN BNL Research Center under its joint tenure track fellowship with Stony Brook University. A. Schäfer is supported by DFG (SFB-TRR 55). Support from the U.S. Department of Energy through the TMD Topical Collaboration is acknowledged.

[1] D. W. Sivers, Phys. Rev. D **41**, 83 (1990).
[2] D. Boer and P. Mulders, Phys. Rev. D **57**, 5780 (1998).
[3] A. Puckett, *Proc. Sci.*, QCDEV2015 (2015) 029.
[4] S. Pisano, Eur. Phys. J. Web Conf. **85**, 02033 (2015).
[5] A. Bazilevsky (RHIC Spin Collaboration), J. Phys. Conf. Ser. **678**, 012059 (2016).
[6] A. Accardi *et al.*, Eur. Phys. J. A **52**, 268 (2016).
[7] P. Hägler, B. Musch, J. Negele, and A. Schäfer, Europhys. Lett. **88**, 61001 (2009).
[8] B. U. Musch, P. Hägler, J. W. Negele, and A. Schäfer, Phys. Rev. D **83**, 094507 (2011).
[9] B. Musch, P. Hägler, M. Engelhardt, J. Negele, and A. Schäfer, Phys. Rev. D **85**, 094510 (2012).
[10] C. Allton *et al.* (RBC/UKQCD Collaboration), Phys. Rev. D **78**, 114509 (2008).
[11] R. Edwards, B. Joó, and K. Orginos (unpublished).
[12] S. M. Aybat, J. C. Collins, J.-W. Qiu, and T. C. Rogers, Phys. Rev. D **85**, 034043 (2012).
[13] J. Collins, *Foundations of Perturbative QCD* (Cambridge University Press, Cambridge, England, 2013).
[14] J. C. Collins and D. E. Soper, Nucl. Phys. **B194**, 445 (1982).
[15] J. C. Collins and D. E. Soper, Nucl. Phys. **B193**, 381 (1981).
[16] M. Engelhardt, P. Hägler, B. Musch, J. Negele, and A. Schäfer, Phys. Rev. D **93**, 054501 (2016).
[17] G. S. Bali, B. Lang, B. U. Musch, and A. Schäfer, Phys. Rev. D **93**, 094515 (2016).
[18] T. Ishikawa, Y.-Q. Ma, J.-W. Qiu, and S. Yoshida, arXiv: 1609.02018.
[19] J.-W. Chen, X. Ji, and J.-H. Zhang, Nucl. Phys. **B915**, 1 (2017).
[20] J.-W. Chen, T. Ishikawa, L. Jin, H.-W. Lin, Y.-B. Yang, J.-H. Zhang, and Y. Zhao, arXiv:1706.01295.
[21] C. Alexandrou, K. Cichy, M. Constantinou, K. Hadjiyiannakou, K. Jansen, H. Panagopoulos, and F. Steffens, Nucl. Phys. **B923**, 394 (2017).
[22] X. Ji, Phys. Rev. Lett. **110**, 262002 (2013).
[23] H.-W. Lin, J.-W. Chen, S. D. Cohen, and X. Ji, Phys. Rev. D **91**, 054510 (2015).
[24] C. Alexandrou, K. Cichy, V. Drach, E. Garcia-Ramos, K. Hadjiyiannakou, K. Jansen, F. Steffens, and C. Wiese, Phys. Rev. D **92**, 014502 (2015).
[25] J.-W. Chen, S. D. Cohen, X. Ji, H.-W. Lin, and J.-H. Zhang, Nucl. Phys. **B911**, 246 (2016).
[26] C. Alexandrou, K. Cichy, M. Constantinou, K. Hadjiyiannakou, K. Jansen, F. Steffens, and C. Wiese, Phys. Rev. D **96**, 014513 (2017).
[27] B. Yoon *et al.*, Phys. Rev. D **95**, 074508 (2017).
[28] M. Constantinou and H. Panagopoulos, Phys. Rev. D **96**, 054506 (2017).
[29] J. Green, N. Hasan, S. Meinel, M. Engelhardt, S. Krieg, J. Laeuchli, J. Negele, K. Orginos, A. Pochinsky, and S. Syritsyn, Phys. Rev. D **95**, 114502 (2017).
[30] S. Syritsyn, J. Bratt, M. Lin, H. Meyer, J. Negele *et al.*, Phys. Rev. D **81**, 034507 (2010).
[31] R. Tangerman and P. Mulders, Phys. Rev. D **51**, 3357 (1995).
[32] M. G. Echevarria, A. Idilbi, Z.-B. Kang, and I. Vitev, Phys. Rev. D **89**, 074013 (2014).

[33] J. Gao, M. Guzzi, J. Huston, H.-L. Lai, Z. Li, P. Nadolsky, J. Pumplin, D. Stump, and C.-P. Yuan, Phys. Rev. D **89**, 033009 (2014).
[34] V. Barone, S. Melis, and A. Prokudin, Phys. Rev. D **81**, 114026 (2010).
[35] V. Barone, S. Melis, and A. Prokudin, Phys. Rev. D **82**, 114025 (2010).
[36] T. Bhattacharya, V. Cirigliano, S. Cohen, R. Gupta, A. Joseph, H.-W. Lin, and B. Yoon (PNDME Collaboration), Phys. Rev. D **92**, 094511 (2015).
[37] R. G. Edwards and B. Joó (SciDAC, LHPC, UKQCD Collaborations), Nucl. Phys. B, Proc. Suppl. **140**, 832 (2005).